Citation: Murali-Girija, M., Koukouvinis, F., Karathanassis, I. K. & Gavaises, M. (2019). Numerical simulation of three-phase flow in an external gear pump using immersed boundary approach. Applied Mathematical Modelling, 72, pp. 682-699. doi: 10.1016/j.apm.2019.03.022

Numerical simulation of three-phase flow in an external gear pump using immersed boundary approach

Murali-Girija Mithun*[1], Phoevos Koukouvinis, Ioannis K Karathanassis, Manolis Gavaises

School of Mathematics, Computer Science and Engineering, City, University of London, Northampton Square EC1V 0HB, UK

Abstract

This paper presents a three-phase fully compressible model applied along with an immersed boundary model for predicting cavitation occurring in a two dimensional gear pump in the presence of non-condensable gas (NCG). Combination of these models is capable of overcoming numerical challenges such as modelling the contact between the gears and simulating the effect of NCG in cavitation. The model accounting for the effect of NCG also has broader applicability, since gas dissolved in liquids can come out of the solution when exposed to low pressures; this plays a significant role in the pump performance and cavitation erosion. Here the simulation results are presented for the gear pump at different operating conditions including the contact between gear, gear RPM and % of NCG; their effects on performance and cavitation is demonstrated. The results suggest that modelling the contact between the gears play a role in the cavitation prediction inside the gear pump. An increase in cavitation is observed when the contact is modelled even for the small pressure difference considered between the inlet and outlet. An increase in the RPM of the gears also results in increased cavitation within the pump, whereas an increase in the percentage of NCG content by a small amount can reduce the cavitation to a greater extent. This reduction is due to the expansion of the gas at a lower pressure which recovers the pressure and prevents or delays the phase-change process of the working fluid. The fluctuations in the outflow rate is also found to increase when the gears are in contact and also with increasing gas content.

Keywords: three-phase flow, cavitation, non-condensable gas, compressible flow, gear pump, barotropic, immersed boundary

---

*Corresponding author
Email address: `mithun.murali-girija.2@city.ac.uk` (Murali-Girija Mithun*)

Nomenclature

c	Speed of sound
B	Bulk modulus
V_n	Nozzle mean velocity
p	Pressure
F	Body forces
t	Time
N	Stiffness of Tait Equation
C_{gas}	Constant of an isentropic process for air
C_{vap}	Constant of an isentropic process for vapour
We	Weber number
l_c	Characteristic length
	Greek Symbols
ρ	Density
σ	Surface tension
α	Volume fraction
γ	Heat capacity ratio for air
κ	Heat capacity ratio for vapour
u	Velocity
S_{ij}	Strain rate tensor
τ	Non-dimensional time
μ	Kolmogorov length scale
τ_μ	Kolmogorov time scale
∇	Differential operator
λ_g	Taylor length scale
μ_t	Turbulent viscosity
τ_{ij}	Sub-grid scale stress
$\rho_{sat,l}$	Saturation density
$p_{sat,l}$	Saturation pressure
δ_{ij}	Kronecker delta
ν	Kinematic viscosity
	Subscripts
v	Vapour
g	Gas
l	Liquid
i, j, k	Cartesian indices

1. Introduction

Gear pumps are rotary displacement machines commonly used in a wide range of automotive, air-conditioning, aviation and other industrial/hydraulic applications due to their versatility along with their simple design and high structural reliability. A gear pump consists of two rotating gears; a drive gear which receives its power from a drive shaft and a driven gear. They work on the fundamental principle of volumetric displacement and can operate over a wide range of conditions by varying their size and rotational speed. To achieve this, a thorough understanding of the flow inside the pump and tubing system is essential. An efficient pump can not only save cost by reducing the energy wasted but also protect the environment by reducing the carbon footprints. To meet the modern trend of designing compact pumps with higher pressure ratios, the pumps must be operated at higher rotational speeds. This increases noise and vibrations significantly in addition to compromising efficiency due to hydrodynamic effects. More often, pumps are one of the major contributors to the system noise, not only due to their moving parts but also due to the pressure pulsations induced by the fluid flow (fluid-borne noise). This is further enhanced if cavitation is occurring during the pump operation. Cavitation occurs when the fluid pressure drops below the vapor pressure locally during the fluid flow. Cavitation in the pump may lead to many undesirable effects apart from noise and vibration, such as erosion (surface pitting) and loss of efficiency leading to excessive consumption of energy.

Despite their significant importance and the massive contribution to the energy consumption, relevant design tools are based mainly on experimentation, trial-and-error guidelines and more recently on simplistic simulation tools. The initial studies in this front were based on graphical [1] or theoretical approaches [2, 3]. Other numerical studies focusing on modeling gear pumps are also available; however, modeling of such a pump is not so trivial despite the pump's simple design. With the recent advancement in engineering and computational technologies, more advanced models capable of performing complex, CFD simulations have been developed. One of the popular but simple approaches for modeling gear pump using lumped parameters can be found in [4, 5]. In their model (HYGESim), the fluid dynamics and the mechanical gear motion are modelled using AMESim®, and the lateral gaps are modelled using CFD, and these models are coupled together with many other sub-models to include cavitation, material erosion and the lateral motion of the gears.

On the other hand, a complete CFD simulation of the gear pump poses a major challenge concerning numerical meshing of gears with small clearances and solid-to-solid contact between the gears. In addition, the modelling requires a dynamic mesh that can adapt to the rotation of the gears without losing the mesh quality. These issues in mesh handling have been a research focus for the past few decades. A superposition method where the stationary and moving regions are meshed separately and the data is interpolated between these meshes during the simulation was employed by [6]. The interpolation between the mesh was a critical step in their method. An arbitrary Lagrangian-Eulerian approach using a pseudo-pressure operator for describing the nodal velocity is presented in [7]. They applied their model on a two-dimensional lobe pump and an external gear pump with an incompressible flow assumption. One limitation of this model according to [8] was the limited control over the mesh in the clearance region due to the automatic re-meshing. An alternative method called FMALE (fixed mesh

ALE) was proposed by [8], in which the evolving geometry is meshed a priori as opposed to re-meshing in the classical ALE. They employed 10 different meshes over a gearing period and used an algorithm for interpolating the data between the time-steps. This approach ensured that the mesh quality is maintained. However, the limitation of this model was that the time-step size is directly related to the number of mesh instances considered in a period. In order to have smaller time-steps, more mesh instances are required which is expensive; on the other hand, if fewer mesh instances are used, a larger time-step is needed and therefore the interpolation between the mesh at two consecutive time-instants can lead to numerical errors. Even though the primary objective of their study was to estimate the suction side pressure distribution to avoid cavitation, no cavitation model was used. The occurrence of cavitation was linked to the pressure values below the fluids vapour pressure, as obtained from the single-phase analysis. In another study, a dynamic mesh approach using an unstructured mesh that deforms and re-mesh to accommodate the gear motion as implemented in Ansys Fluent® was employed by [9]. This approach can be expensive if the mesh count is large and smaller time-step values are used, which is typically the case for gear pumps where frequent adaption of the mesh is required to maintain the mesh quality. A hybrid between the deform/re-mesh approach of [9] and the mesh replacement approach of [8] was employed by [10]. Their study was focused on the flow field in the inlet chamber. They performed two-dimensional simulations using both laminar and RANS flow approximations with various two-equation turbulence models. They concluded that the modelling of contact between the teeth and a proper choice of turbulence model is essential to capture the flow fluctuations which are responsible for the pressure ripples, noise and vibration. A three-dimensional simulation of the external gear pump using OpenFOAM toolkit was recently reported by [11]. Since this study was dedicated to mesh manipulation and modelling gear contacts, cavitation and turbulence were not taken into account.

Despite its importance, none of the works described above considers the effect of cavitation in their studies. To the best of authors' knowledge, the first CFD work to consider cavitation in a gear pump was reported by [12]. They considered a two-dimensional gear pump to study the influence of different parameters such as suction chamber geometry and gear RPM on cavitation and volumetric efficiency. They compared their results obtained using different cavitation models with experimental results to test the applicability of each model. In the follow-up work, the effect of operating pressure on pump performance in the presence of cavitation was studied by [13]. They reported that the impact of suction side cavitation on the outlet flow and pressure ripples observed at the outlet for low pressure (10bar) disappear when a mean pressure jump of 100bar is applied. However, no significant change in the inlet flow and morphology of cavitation is observed with the increase in operating pressure. In their study, unlike the approach of [10], where a tiny wall was defined to model the contact between the gears that will deform with the gear rotation until the new mesh replaces it, the authors of [13] modelled the gear contact by increasing the dynamic viscosity to a higher value at the contact location. According to [13], the approach of [10] produces numerical errors when cavitation is considered. A recent study considering cavitation in the numerical analysis of a 3D gear pump can be found in [14]. They used the commercial code PumpLinx® for their simulation and validated their results against the experimental data from the pump manufacturer. Their cavitation model was based on the work of [15] which consider the effect of a finite amount of non-condensable gas. To have a better prediction of the volumetric efficiency, the authors have considered all the leakage paths and grooves in their model. However, they did not consider the contact between the gears.

It has been pointed out in the literature by many authors e.g. [12, 16] that the interpolations involved while using a traditional re-meshing/deforming approach or a mesh replacement approach could lead to numerical errors especially while solving for multi-phase flows and with high gear RPM. Moreover, they are computationally expensive due to the small time-step requirements for maintaining the mesh quality in small clearances. To overcome these complexities, approaches such as overset mesh, which uses a background mesh and many component meshes have been employed in the past [17] for simulating turbo-machinery. Even though this approach ensures better mesh quality, the numerical errors arising from the interpolation of data between the base and component mesh cannot be avoided. From the personal experience of the authors, modeling clearance between the gears is also challenging since the data interpolation requires at least four overlapping cells between the background and component mesh. An alternate approach that is becoming increasingly popular for such simulations is the immersed boundary method. This approach was initially utilized for biological applications [18] with flexible geometries. Later, this approach was modified and used for rigid body simulations by other researchers [19, 20]. A detailed review of the immersed boundary approaches can be found in [21, 22]. In a recent study, the immersed solid approach implemented in Ansys CFX® was employed by [16] for modeling a three-dimensional gear pump operating at very high speed (10,000 RPM). They claim that the use of this method simplified their numerical simulation setup and reduced the computation time to a great extent. Their model was validated against the experimental data for flow rate measurements. They concluded that the dominant geometrical parameters that influence the pump flow rate are the tip and the lateral clearances. The limitation of their work is that it was not applied in multiphase or variable density flows.

Motivated by the above discussions, in the present study, an immersed boundary approach, which is developed and implemented by the authors in Ansys Fluent® using a user-defined function (UDF), is employed. This approach allows a faster and easier way of modeling gear pump without any mesh interpolation. Moreover, the use of immersed boundary approach enabled the modeling of gear contact more easily without any additional numerical efforts. In addition to that, the present study also considers the effect of cavitation along with the presence of non-condensable gas using a fully compressible three-phase cavitation model. Modeling of non-condensable gas is essential in applications like aircraft fuel pumps, where the inlet tank is vented to lower ambient pressure at higher altitudes. At this lower pressure, according to Henry's law, the dissolved gas in the fuel may get released and present as non-condensable gas (NCG) at the suction side of the pump. It is well known that the presence of impurities such as NCG can reduce the tensile strength of the liquid and can advance cavitation formation [23]. Also, the presence of highly compressible gas phase at the suction can adversely affect the efficiency of the pump. In this study, the turbulence in the flow is modelled using the SST k-ω model with proper correction for the turbulent viscosity [24] to circumvent the overestimation of turbulent dissipation in the two-phase region, which is a typical problem in two-equation turbulence models. To the best of the authors' knowledge, this is the first work to consider the effect of non-condensable gas in a gear pump simulation and one of the few studies where the cavitation is considered along with the compressibility of all the phases. The developed three-phase model and the immersed boundary method will aid the pump designers in developing efficient gear pumps by taking into account more realistic physics into their numerical model.

The structure of this paper is outlined as follows: The numerical method used for the three-phase equilibrium model and the immersed boundary approach are discussed in the next section, followed by the simulation setup for the gear pump. The major findings from the simulations are then shown in the results and discussion section with the main conclusions summarised at the end.

2. Numerical model

The numerical formulation used for modelling three-phase cavitation and the moving boundary is explained in this section.

2.1. Governing Equations

The three-phase flow is governed by the continuity and momentum equations describing the motion of the mixture. The averaged form of the governing equations employed for the RANS (Reynolds Averaged Navier-Stokes) simulations are:

$$\frac{\partial \rho_m}{\partial t} + \frac{\partial \rho_m u_j}{\partial x_j} = 0 \tag{1}$$

$$\frac{\partial \rho_m u_i}{\partial t} + \frac{\partial \rho_m u_i u_j}{\partial x_j} = -\frac{\partial p}{\partial x_j} + \frac{\partial}{\partial x_j}\left[\mu\left(\frac{\partial u_i}{\partial x_j} + \frac{\partial u_j}{\partial x_i} - \frac{2}{3}\delta_{ij}\frac{\partial u_l}{\partial x_l}\right)\right] + \frac{\partial}{\partial x_j}(-\rho_m \overline{u_i' u_j'}) + f_{IB} \tag{2}$$

where ρ_m is the mixture density, μ is the molecular viscosity, p is the pressure, f_{IB} is the forcing term for the immersed body and $(-\rho_m \overline{u_i' u_j'})$ is the Reynolds stresses which are modelled using Boussinesq hypothesis; Eq. (3):

$$-\rho_m \overline{u_i' u_j'} = \mu_t\left[\frac{\partial u_i}{\partial x_j} + \frac{\partial u_j}{\partial x_i}\right] - \frac{2}{3}\left[\rho_m k + \mu_t \frac{\partial u_k}{\partial x_k}\right]\delta_{ij} \tag{3}$$

where, μ_t is the turbulent viscosity, and δ_{ij} is the Kronecker delta.

In this study, the turbulence is modelled using a *SST* k-ω model which takes into account the transport of turbulent shear stress. The transport equations for the turbulent kinetic energy (k) and specific dissipation (ω) are given in Eq. (4) and (5) respectively.

$$\frac{\partial}{\partial t}(\rho_m k) + \frac{\partial}{\partial x_i}(\rho_m k u_i) = \frac{\partial}{\partial x_j}\left(\Gamma_k \frac{\partial k}{\partial x_j}\right) + G_k - Y_k + Su_k \tag{4}$$

$$\frac{\partial}{\partial t}(\rho_m \omega) + \frac{\partial}{\partial x_j}(\rho_m \omega u_j) = \frac{\partial}{\partial x_j}\left(\Gamma_\omega \frac{\partial \omega}{\partial x_j}\right) + G_\omega - Y_\omega + Su_\omega \tag{5}$$

where Γ, G, Y and Su are the effective diffusivity, turbulent production, dissipation and user-defined source terms. The definitions of Γ, G, Y can be found in [25].

In addition to the correction implemented for eddy-viscosity in the SST model to avoid the over prediction of its value, an additional correction for the density term (ρ in the eddy-viscosity equation is replaced with $f(\rho)$) is implemented in the calculation of eddy-viscosity to compensate for the compressibility of the liquid-vapour mixture [24] as given in Eq. (6) and (7):

$$f(\rho) = \rho_v + (1-\alpha)^{10}(\rho_l - \rho_v) \tag{6}$$

$$\mu_t = f(\rho)\frac{a_1 k}{max(a_1\omega, SF_2)} \tag{7}$$

where, α is the vapour volume fraction, the subscript l and v refers to liquid and vapour, a_1=5/9, S=$\sqrt{(2S_{ij}.S_{ij})}$ with S_{ij} being the strain rate tensor and F_2 is the blending function [26].

The source terms f_{IB}, Su_k and Su_ω in Eqs. (2), (4) and (5) will account for the immersed body, and their implementation is given in the next section.

2.2. Immersed boundary (IB) model

Due to the small clearances and the contact between the gears, the canonical body fitted grids with re-meshing/deforming approaches can be computationally expensive and inefficient. In an immersed boundary method (IBM), the presence of a body is represented using a forcing term in the momentum equation. The IB method used in this study is based on the *continuous forcing* approach [18, 22] where the forcing term (f_{IB}) is added to the continuous form of momentum equation as shown in Eq. (2). The term f_{IB} is the source term that forces the flow to follow the boundaries of the immersed body. This force is proportional to the difference in flow velocity ($\bar{u}$) and the target body velocity ($\bar{U}_{IB}$; which is the velocity of the immersed body). The formulation of the forcing term is given in Eq. (8):

$$f_{IB} = -\frac{\rho_m C}{dt}\alpha_{IB}(\bar{u} - \bar{U}_{IB}) \tag{8}$$

In the above equation, C is an arbitrary coefficient which can be tuned to adjust the strength of the immersed body velocity ($C = 1$ in this study), dt is the time step and α_{IB} is the masking function which takes a value of 1 if the cell is inside the immersed body (solid) and 0 if the cell is outside (fluid). Any value between 0 and 1 refers to a cell which is partially occupied by the wall. For calculating the mask function in each cell, the wall normal distance of each cell nodes from the immersed boundary points is estimated, and the IB point with the minimum distance is identified. The formulation of this can be represented using Eq. (9):

$$d_{n,IB} = (\bar{x}_n - \bar{X}_{IB}).n_{IB} \qquad if \qquad min(|\bar{x}_n - \bar{X}_{IB}|) \tag{9}$$

where $\bar{x}_n$ and $\bar{X}_{IB}$ are the coordinates of the cell node and immersed boundary point, n_{IB} is the normal to the wall. The distance from the immersed body to the cell is estimated as the average of node distances Eq. (10):

$$d_{c,IB} = \frac{\sum\limits_n d_{n,IB}}{n} \tag{10}$$

After estimating the distance function from Eq. (9), the mask function α_{IB} in Eq. (8) is calculated using Eq. (11):

$$\alpha_{IB} = \frac{\sum\limits_n [-min(d_{n,IB}, 0)]}{\sum\limits_n |d_{n,IB}|} \tag{11}$$

When the immersed body is moved, the Eulerian cells inside the immersed body should have the same velocity as the body. This is calculated using Eq. (12):

$$\bar{U}_{IB} = \frac{d\bar{x}}{dt} + \omega_{IB} \times (\bar{x}_c - \bar{x}_{IB,cm}) \tag{12}$$

where ω_{IB} is the angular velocity, $\bar{x}_c$ is the cell centre and $\bar{x}_{IB,cm}$ is the coordinates for the centre of mass of the immersed body. The new position for the immersed boundary points and the boundary normal after the rotation are then computed using Eq. (13) and (14):

$$x_{IB}^{new} = x_{IB,cm}^{new} + RM(\theta)\big[x_{IB,cm}^{old} - x_{IB,cm}^{new}\big] \tag{13}$$

$$n_{IB}^{new} = RM(\theta)\big[n_{IB}^{old} - n_{IB}^{new}\big] \tag{14}$$

where, n is the normal vector to the immersed boundary wall, and $RM(\theta)$ is the rotation matrix defined in Eq. (15):

$$RM(\theta) = \begin{bmatrix} \cos(\theta) & \sin(\theta) & 0 \\ -\sin(\theta) & \cos(\theta) & 0 \\ 0 & 0 & 1 \end{bmatrix} \tag{15}$$

To obtain the gear geometry as immersed boundary points and the surface normal, the geometry was first meshed in a meshing software (Gambit® in this study) and exported as a neutral file (*.neu). The centroid of each cell and the surface normal at the cell centroid, the barycentre location of each cell and the corresponding surface normal are computed. These data are then imported into the solver using a user-defined function, and the new coordinates for the immersed boundary points and surface normal are updated according to the formulations explained before to accommodate the gear rotation.

The source terms in the turbulence equations, Eq. (4) and (5) are defined such that it satisfies the conditions of $k = 0$ and $\omega \to \infty$ (10^{15} in this study) close to the wall where there is less turbulence. This is achieved by defining the source terms for turbulent kinetic energy and specific dissipation as:

$$Su_k = -\frac{\rho_m C}{dt} \alpha_{IB}(k - 0) \tag{16}$$

$$Su_\omega = -\frac{\rho_m C}{dt} \alpha_{IB}(\omega - 10^{15}) \tag{17}$$

In the present study, the elastic deformation of the gears at the contact zone is not considered as this deformation is negligible for the metallic gears assumed in the present study. However, for applications in metal-polymer gear or in other biomedical applications where the boundaries are flexible, the forcing function in the IBM formulation can be modified to include the elastic deformation.

2.3. Three-phase model

The cavitation model used in this study is based on the homogeneous equilibrium assumption which uses a barotropic equation of state for modelling the pressure-density relationship of each phase. The barotropic relation employed here is a piecewise function as given in Eq. (18):

$$p = \begin{cases} B\left[(\frac{\rho}{\rho_l})^N - 1\right] + p_{sat,l} & \rho \geq \rho_l \\ \frac{c_v^2 c_l^2 \rho_l \rho_v (\rho_v - \rho_l)}{c_v^2 \rho_v^2 - c_l^2 \rho_l^2} \ln\left(\frac{\rho}{c_l^2 \rho_l (\rho_l - \rho) + c_v^2 \rho_v (\rho - \rho_v)}\right) + p_{ref} & \rho_v \leq \rho \leq \rho_l \\ C_{vap} \rho^\kappa & \rho \leq \rho_v \end{cases} \tag{18}$$

where B and N are the bulk modulus and the stiffness of the liquid, subscripts l and v refer to pure liquid and vapour phases, c is the speed of sound, ρ is the density. $p_{sat,l}$ and p_{ref} are tuned to have a continuous variation of pressure and density between the liquid and mixture phase. C_{vap} and κ are the isentropic constant and heat capacity ratio of pure vapour.

This formulation corresponds to fully compressible media; a modified form of Tait equation is utilized for modeling liquid compressibility: the pure vapor phase is modelled using isentropic gas equation. The pressure-density relationship for the mixture phase is derived by integrating Eq. (19) for an isentropic process with the speed of sound defined using the Wallis formulation. The values of the parameters in Eq. (18) are listed in Table. 1. Water at room temperature and standard sea-level pressure are considered as the working fluid in this study since its thermodynamic properties are easily available.

$$c^2_{Wallis} = \left(\frac{\partial p}{\partial \rho}\right)_s \tag{19}$$

The third phase, the non-condensable gas (air) is modelled as an additional phase with no mass transfer between the liquid/ vapor phase using the mixture approach similar to that of [27] is implemented in the solver, where a transport equation for the volume fraction of the gas phase (α_g) is solved. The barotropic relationship for the non-condensable gas is based on the isentropic gas equation as given in Eq. (20):

$$p = C_{gas}\rho^{\gamma} \tag{20}$$

where C_{gas} is the isentropic gas constant, and γ is the heat capacity ratio for air.

The three-phase mixture density and the volume fraction of the vapour phase is calculated using Eq. (21) and Eq. (22) respectively:

$$\rho_m = (1 - \alpha_g)\rho_{lv} + \alpha_g\rho_g \tag{21}$$

$$\alpha_v = \frac{(\rho_l - \rho_{lv})}{(\rho_l - \rho_v)} \tag{22}$$

where the subscripts m, lv, v and g refers to the three-phase mixture, barotropic fluid, pure vapour and non-condensable gas phases respectively and α is the volume fraction.

The barotropic model presented above was recently used by [29], [30] for studying primary atomization from a step-nozzle. However, in their study,

Table 1: Thermodynamic properties for water, vapour and gas at 20^{o}C [28]

Liquid properties			Vapour properties			Gas properties		
B	3.07	GPa	C_{vap}	27234.7	Pa/(kg/m^3)^n	C_{gas}	75267.8	Pa/(kg/m^3)
N	1.75	–	κ	1.327	–	γ	1.4	–
ρ_l	998.16	kg/m^3	ρ_v	0.0173	kg/m^3			
c_l	1483.26	m/s	c_v	97.9	m/s			
$p_{sat,l}$	4664.4	Pa	$p_{sat,v}$	125	Pa			
μ_l	1.02	mPa.s	μ_v	9.75	μPa.s	μ_g	0.178	μPa.s

the three-phase model was closed using a volume of fluid approach (VoF) with sharp interfaces that do not allow interpenetration of phases, unlike the diffused interface mixture model used in the present study. The formulation of the barotropic model is repeated in this study for the sake of completeness and to make it easier for the readers to follow.

3. Simulation Setup

Simulations have been performed for a 2D gear pump; the pump geometry is publicly shared by [31] as shown in Fig. 1a. The only difference in geometry between [31] and the present study is that the curved shoulders at the inlet and outlet are replaced with sharp ones in this work. The most difficult features in a gear pump simulation, as explained before are the modeling of small clearances and the contact between the gears while maintaining a reasonable mesh quality. In the present simulation, the application of the IB method has made the implementation of these tasks more manageable. To model the contact between the gears, one of the gears is rotated by a small angular position so as to make the gear surfaces touch each other before exporting the coordinate positions of the gears into immersed boundary code. In Fig. 2, the clearances between the gears and between the gears and casing along with the contact between gears are highlighted using immersed boundary points superimposed on the background mesh. An additional refinement for the numerical mesh is provided at the location where the two gears come in contact as highlighted in Fig. 1. This refinement ensures sufficient grid elements in the clearances to capture the leakage flow between the gears. With this refinement and the addition of boundary layer refinement to limit the y^+ values below 5 in most of the domain for the extreme condition considered, the total mesh count reaches up to 0.5 million cells.

Constant absolute pressure boundary conditions have been applied to the inlet and outlet boundaries. In all the cases considered in this study, a relatively low pressure jump is applied between the inlet and outlet (∼10 bar), similar to the numerical study of [12].

All simulations have been performed using 2 CPU's with 8 cores each (16 cores) having a clock speed of 1.95 GHz on a Linux cluster. The elapsed wall-clock time for one pitch rotation of the gears at 2000 RPM was approximately 6 hours.

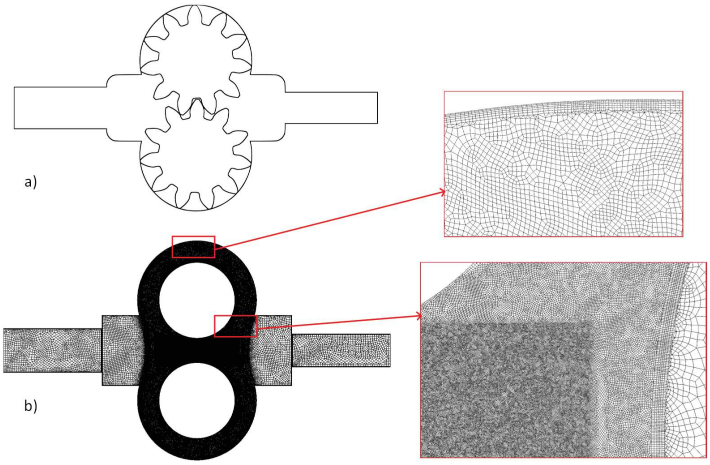

Figure 1: a) Line diagram of the gear pump from [31] and b) the computational mesh for immersed boundary simulation

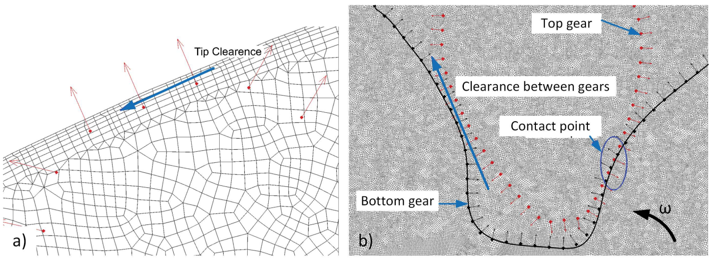

Figure 2: Modelling of a) tip clearances and b) clearance and the point of contact between the gears

4. Results and Discussion

Due to the two-dimensional approximation used in this study, the volumetric efficiency and the flow rates reported may not replicate the values observed in a real gear pump since the leakage paths, side porting and the relief grooves cannot be modelled in two dimensions. However, since the primary objective of this work is to present a numerical model that can handle three-phases in conjunction with an immersed boundary method for complex gear motion, the approximations used for simplifying the problem can be justified. Validation of the numerical model is performed on two different cases, a two-dimensional rotating cross (see the supplementary material S0) and also with some experimental works on gear pump available in the literature. In Fig. 3, the streamlines observed by [10] using TRPIV are compared with the current numerical study. The flow field and the velocity profile plotted in Fig. 3 shows a good correlation with the experimental values. In addition to this, a qualitative comparison is also made for the cavitation predictions at two different gear RPMs as shown in Fig. 4. It can be observed that the locations of the cavitation predicted from the simulations correlate very well with the vortex core observed in the gap between the teeth at the suction chamber observed in the experimental work of [33] for both the cases considered.

In the results that follow, the pressure is made non-dimensional using the inlet pressure of 1bar, time using the term T_g defined as $T_g = 11 \cdot RPM/60$, and the non-dimensional velocity is defined as $V/(r_g \omega_z)$, where r_g is the radius of the gear and ω is the angular velocity in rad/sec.

4.1. Effect of gear contact

The effect of contact between the gears on cavitation and pump performance is studied by comparing two cases, one with a clearance of 74μm (which is very small compared to the distance between the gear centres which is 45.1mm) between the gears and the other condition when gears are in contact. Unlike the unitary contact ratio (a ratio that defines the average number of teeth that are in contact with the mating gear during a period in which a tooth comes and goes out of contact) studied in the simulations of [12], in the present study, the contact between the gears occurs at two locations, i.e. before the first contact separates, the next pair of gears come in contact. This creates a region isolated from the inlet and outlet where very high pressures are expected in a two-dimensional simulation. In Fig. 5, a comparison of the development of pressure over a gearing period for two conditions considered are shown. A gradual rise in pressure from the inlet towards the outlet is observed when a continuous clearance is present between the gears, see Fig. 5a. As the gear rotates, the fluid inside the pockets are compressed, and the liquid on the high-pressure side leaks towards the inlet through the small clearances as shown in Fig. 5(b, c) and Fig. 6(b, c). The acceleration of this leakage flow through the clearance creates a low-pressure zone and results in the formation of cavitation (Fig. 7). This cavity acts as a fictitious contact point that separates the inlet chamber from the outlet as also observed by [12]. A sudden jump in absolute pressure across this fictitious contact can be observed in Fig. 5(b, c). The cavitation occurring in the clearances is highlighted using red circles in Fig. 7. On the other hand, when the contact between the gears are modelled, the first contact point (Contact-1) act as the barrier between the inlet and outlet which produces a sudden pressure jump across this point as can be seen from Fig. 5(a' - c'). Unlike the first case, the solid-solid contact does not allow flow across it, and hence no cavitation is observed at contact location (Fig. 6(b', c') and Fig. 7(b', c')). When the gears cross half pitch rotation, the second contact is established, trapping a volume of fluid between the two contacts; Fig. 5c'. Further rotation of the gear raises the pressure in the trapped volume up to 30-40 times the inlet pressure Fig. 5(c'2). This region is of particular interest in many studies (for, e.g. ([11]; [34]; [33])) as this pressure rise can produce noise and vibration in the pump. In a real gear pump, relief grooves are provided to drain this trapped fluid to the inlet chamber to avoid excessive vibration arising from the high-pressure fluid loading on the gears. Unlike the previous case, i.e. without contact, cavitation does not appear in this region due to the pressurised fluid in the trapped volume (Fig. 7d) when the gears are in contact. While this is true for 2D simulations, in a real gear pump with relief grooves, the high-velocity jet from the trapped volume towards the inlet chamber through grooves can lead to erosion due to jetting. The contact between the gears at one side provides an additional clearance (t2 $>$ t1) in the backlash and hence a low-velocity jet is produced at the outlet chamber, compared to the case with clearance (Fig. 6e and e'). An overall increase in cavitation is observed when the gears are in contact. This increase is mainly attributed to the increase in cavitation just ahead of the contact point where the pressure is much lower due to the isolation of the of high-pressure side from inlet by the contact point compared to the case without contact where relatively higher pressures are realised due to the continuous connection between inlet and the outlet chamber. This can be confirmed by comparing the total vapour generation over time for the two cases. In Fig. 8a, the time evolution of the area integral of vapour volume fraction is shown for the two cases considered. This quantity is used as a measure of cavitation generation over time. The result of the integration plotted in Fig. 8a clearly shows an increase in cavitation volume (assuming unity depth) when the gears are in contact, with the mean value of vapour volume fraction at 0.19% against 0.14% without contact. The mean value of the mass flow rate plotted in Fig. 8c also increases approximately by ∼4.5% when the gears are in contact. Such an increase in flow rate with contact between the gears was also acknowledged by [10] for a unity contact ratio. They also reported that the flow fluctuation increases with the contact due to the water hammer effects caused by the sudden opening and closing of the inner teeth chamber to both the outlet and inlet. Similar to their findings, the fluctuations in the flow along with the breakage of temporal symmetry are also observed in the present simulation. The compressibility of the fluid along with the nature of gear pump operation produces this flow fluctuations which are often a source of the fluid-borne noise. The fluctuations observed in the inlet is almost half of that of the gearing period, due to the suction produced by both gears. The additional higher frequency oscillations observed in the inlet flow rate signal can be associated with cavitation occurring in the low-pressure chamber. At the outlet, the flow rate fluctuation matches with the frequency of a gearing period. A comparison of the percentage difference between the maximum outflow rate at any instant to the mean outflow rate shows a 5.5% difference when the gears are not in contact whereas this is as high as 12% when they are in contact.

4.2. Effect of gear RPM

To study the effect of gear RPM on cavitation, simulations are performed for three different rotation speeds; 500, 1000 and 2000 RPM. The results presented from this point onwards consider a contact ratio greater than unity unless mentioned otherwise. In Fig. 9, a comparison of cavitation occurring in the inlet chamber, represented using the contours of vapor volume fraction over a period ($1/11^{th}$) of gear rotation is shown. It is evident from the figure that the cavitation volume increases with the increase in gear RPM. At lower RPM, the formation of cavitation is observed in the gap between the gears where they expand in the inlet chamber. The strong vortical structures generated due to the expanding gears initiates this cavitation at its low-pressure core. At 1000 RPM, in addition to the vorticity induced cavitation in the expanding volume, cavitation is also formed due to the separation of the flow from the gear tips rotating towards the inlet. A further increase in rotational speed produces stronger vortices and larger separation zones resulting in increased cavitation in the inlet chamber as can be seen in column-3 of Fig. 9. The vortical structures generated in the domain are shown in Fig. 10 at t/T_g =0.5 for comparison. The structures leading to the formation of cavitation between the gears in the inlet zone and the vorticity due to the flow separation can be clearly seen from the figure. In addition to that, vortical structures are also observed at the clearance between the gear and the casing and also at the outlet chamber where the fluid is pushed out. Since the absolute pressure values at these locations are higher, being on the pressure side, cavitation does not occur here.

The area integral of the vapor volume fraction over two gearing periods reported in Fig. 11a, similar to the one presented in the previous sections is used to quantify the cavitation at different RPM. A comparison of this quantity confirms that the minimum cavitation occurs at 500 RPM and the maximum at 2000 RPM, with the addition of cavitation due to flow separation. With an increase in gear RPM, the net flow rate is also increased as can be seen in Fig. 11(b, c). It can be noticed that the maximum amplitude of fluctuations occurs at 1000 RPM, where the cavitation is more dynamic with frequent cavity creation and collapses, and minimum at 500 RPM where only less cavitation occurs. At 2000 RPM, even though the cavitation is much higher, it is less dynamic compared to the 1000 RPM with a continuous presence of stable cavities in the domain. These arguments can once again be confirmed by examining the evolution of vapor volume fraction shown in Fig. 11a which shows maximum fluctuations at 1000 RPM. The RMS and the maximum value of the fluctuating flow rate at different gear RPM are reported in Table. 2. It is found that the percentage deviation between the mean and maximum flow rate reduces with the increase in RPM. This is because, at higher RPM, the gears become closer to replicate as a rotating disc with minimum fluctuations.

The development of the pressure from the inlet to the outlet at 500 RPM at a selected time instant is shown in Fig. 12. The time instant is selected such that two points of contact are established, and the liquid trapped between the contacts is compressed. The figure shows the non-dimensional pressure (p/p_{in}) plotted at different locations along the curve passing from inlet to outlet through the gear pockets (1-15) and through to the meshing zone

Table 2: Mean and fluctuating outflow rate at different RPM

RPM	$\bar{m}_{out}(kg/s)$	$m_{out,RMS}(kg/s)$	$\dot{m}_{max}(kg/s)$	%change $\frac{(\dot{m}_{max}-\bar{m}_{out})}{\bar{m}_{out}} * 100$
500	8.36	8.39	9.71	16.1
1000	18.54	18.59	20.81	12.2
2000	38.47	38.57	41.94	9.0

(5' - 13') as shown in Fig. 12a. The distribution of the pressure follows a stairway step profile along the line (1-15). A similar distribution was also observed by [8] in their numerical simulation. Along the path 5' - 13', which passes through the gear meshing zone, the trapped liquid gets compressed and a sudden jump in pressure between 5' and 6' is observed. The absolute pressure in this region can easily reach up to 30 times the inlet pressure as can be seen from Fig. 12b. The impact of this rise in pressure and the measures to avoid this unintended pressure rise were already discussed in the previous sections. The pressure rise from the inlet to outlet follows a similar trend for all other cases considered in this study, hence it is not shown here.

In Fig. 13, the contours of the pressure and the velocity magnitude at different RPM are shown at t/T_g=0 and 0.5. Jetting of fluid at the outlet chamber during the meshing of gears can be seen from the figure. The velocity of the jet increases with the increase in RPM, and this causes the pressure to drop locally near the gear tips at the outlet chamber as highlighted using blue circles in Fig. 13. Since this is occurring in the high-pressure chamber, the pressure drop is not sufficient to produce cavitation.

4.3. Effect of Non-condensable Gas

The effect of non-condensable gas on cavitation is studied by varying its content in water from 0% to 1% by volume at a constant rotational speed of 2000 RPM. Once again, the quantification of the cavitation corresponding to each NCG content is achieved by taking the area integral of the vapor volume fraction. A comparison of this result is presented in Fig. 14a over two gearing periods. It is observed that the effect of non-condensable gas is to reduce the amount of cavitation. In the absence of non-condensable gas in the fluid, a reduction in local pressure below vapor pressure immediately causes the liquid to change its phase to vapor phase. On the other hand, in a similar situation, if a certain amount of non-condensable gas is present in the liquid, the reduction in local pressure is recovered to a certain extent by the expansion of the highly compressible gas and hence limiting cavitation. The

Table 3: Mean and fluctuating outflow rate for different gas content at 2000 RPM

NCG%	$\bar{m}_{out}(kg/s)$	$m_{out,RMS}(kg/s)$	$\dot{m}_{max}(kg/s)$	%change $\frac{(\dot{m}_{max}-\bar{m}_{out})}{\bar{m}_{out}} * 100$
0%	38.47	38.57	41.94	9.03
0.2%	38.09	38.20	42.20	10.80
1%	38.07	38.28	44.68	17.35

formation of cavitation and the expansion of the NCG at the inlet chamber under different conditions are shown in Fig. 15. The reduction in cavitation with increasing NCG can be appreciated from this figure. In addition, a comparison of vapour contours at 0%, 0.2% and 1% NCG reveals that the core of cavitation remains the same, which is at the core of the vortices, while the spread of the vapour cavity around the core is limited by the expansion of the gas, larger volume fraction of NCG can be seen around the vapour cavities. To verify the effect of NCG on the pump performance, a comparison of the flow rate measurements at inlet and outlet is performed; the results are presented in Fig. 14(b, c). It is observed that the mean flow rate does not change, but the amplitude of the flow fluctuations at the inlet and outlet increases with an increase in NCG content. This increase in fluctuations could be due to the increased compressibility of the mixture in the presence of NCG. The percentage difference between the instantaneous maximum outflow rate and the mean outflow for 0%, 0.2% and 1% are shown in Table. 3. It can be noticed that the percentage change between maximum and mean outflow increases with the increase in NCG content.

5. Conclusions

In this study, a numerical model for predicting cavitation in the presence of non-condensable gas along with an immersed boundary method was developed for modelling three-phase cavitation occurring in a gear pump. Such a model is essential for understanding the flow behaviour inside the pump in detail at different operating conditions. These details will help in efficient designing of pumps with reduced cavitation and associated energy losses. The multiphase flow model used in this study is fully compressible and utilizes the k-ω-SST turbulence model with a user-defined correction for the turbulence viscosity. The cavitation and the IB models are validated against numerical and experimental results from the literature. After validating the numerical model, simulations are performed on a 2D gear pump model to study the effect of contact between the gears, RPM and the amount of NCG on cavitation formation, development and collapse, as well as on pump performance. A comparison with experiments has shown that the current model could predict cavitation occurring due to vorticity in the suction chamber accurately; use of the immersed boundary approach has made the modelling of contact ratios greater than unity easier. With sufficient refinement, the approach also produces accurate results in less time as compared to other conventional re-meshing methods, as there is no mesh deformation and interpolation of data involved.

It is observed that when the gears are in contact, cavitation occurring in the suction chamber increases due to the isolation of low-pressure side from the high-pressure chamber. As a result, more fluctuations are present in the outlet flow and a slight increase in mean flow rate is also observed as compared to the case without contact. When the contact between the gears occur at more than one location, a volume of liquid is trapped between the gears and it is compressed. The pressure in this trapped volume is observed to rise up to 30-40 times relative to the inlet pressure.

At lower RPM, cavitation is primarily observed at the core of the vortex forming between the gear teeth opening towards the inlet. With an increase in the rotational speed, vapor cavities are additionally formed at the gear tips due to flow separation. Both intensity and the total volume of cavitation increase with the gear RPM. The effect of NCG on cavitation occurring in gears pump was studied for the first time. This study is conducted by varying the gas content in the flowing liquid from 0% to 1% by volume. The results suggest that the presence of NCG reduces the formation of cavitation without having much impact on the average outlet flow rates. However, an increase in fluctuation in the outlet flow is observed with the increase in gas content.

The numerical model presented here is also validated and applied for three-dimensional gear pump simulations with side porting and axial clearances. The result from the 3D gear pump simulations along with the experimental results will be later published as a continuation of this work.

Declaration of conflicting interests

The author(s) disclosed receipt of the following financial support for the research, authorship, and/or publication of this article: The author(s) declared no potential conflicts of interest with respect to the research, authorship and/or publication of this article.

Acknowledgements

This work was carried out in the framework of CaFE project, which has received funding from the European Union Horizon 2020 Research and Innovation programme, with Grant Agreement No 642536.

References

[1] TE Beacham, “High-Pressure Gear Pumps,” Proceedings of the Institution of Mechanical Engineers **155**, 417–452 (1946).

[2] M Borghi, B Zardin, and E Specchia, “External Gear Pump Volumetric Efficiency: Numerical and Experimental Analysis,” SAE Technical Paper , (2009).

[3] ND Manring and SB Kasaragadda, “The Theoretical Flow Ripple of an External Gear Pump,” Journal of Dynamic Systems, Measurement, and Control **125**, 396 (2003).

[4] A Vacca and M Guidetti, “Modelling and experimental validation of external spur gear machines for fluid power applications,” Simulation Modelling Practice and Theory **19**, 2007–2031 (2011).

[5] J Zhou, A Vacca, and P Casoli, “A novel approach for predicting the operation of external gear pumps under cavitating conditions,” Simulation Modelling Practice and Theory **45**, 35–49 (2014).

[6] D Bruce, M Wilson, and S Generalis, “Flow Field Analysis of Both the Trilobal Element and Mixing Disc Zones within a Closely Intermeshing, Co-Rotating Twin-Screw Extruder,” International Polymer Processing **12**, 323–330 (1997).

[7] K Riemslagh, J Vierendeels, and E Dick, “An arbitrary Lagrangian-Eulerian finite-volume method for the simulation of rotary displacement pump flow,” Applied Numerical Mathematics **32**, 419–433 (2000).

[8] G Houzeaux and R Codina, “A finite element method for the solution of rotary pumps,” Computers and Fluids **36**, 667–679 (2007).

[9] W Strasser, “CFD Investigation of Gear Pump Mixing Using Deforming/Agglomerating Mesh,” Journal of Fluids Engineering **129**, 476–484 (2006).

[10] R Castilla, PJ Gamez-Montero, N Ertürk, A Vernet, M Coussirat, and E Codina, "Numerical simulation of turbulent flow in the suction chamber of a gearpump using deforming mesh and mesh replacement," International Journal of Mechanical Sciences **52**, 1334–1342 (2010).

[11] R Castilla, PJ Gamez-Montero, D del Campo, G Raush, M Garcia-Vilchez, and E Codina, "Three-Dimensional Numerical Simulation of an External Gear Pump With Decompression Slot and Meshing Contact Point," Journal of Fluids Engineering **137**, 041105 (2015).

[12] D del Campo, R Castilla, GA Raush, PJ Gamez-Montero, and E Codina, "Numerical Analysis of External Gear Pumps Including Cavitation," Journal of Fluids Engineering **134**, 081105 (2012).

[13] D del Campo, R Castilla, GA Raush, PJ Gamez-Montero, and E. Codina, "Pressure effects on the performance of external gear pumps under cavitation," Proceedings of the Institution of Mechanical Engineers, Part C: Journal of Mechanical Engineering Science **228**, 2925–2937 (2014).

[14] E Frosina, A Senatore, and M Rigosi, "Study of a High-Pressure External Gear Pump with a Computational Fluid Dynamic Modeling Approach," Energies **10**, 1113 (2017).

[15] AK. Singhal, MM Athavale, H Li, and Y Jiang, "Mathematical Basis and Validation of the Full Cavitation Model," Journal of Fluids Engineering **124**, 617 (2002).

[16] Y Yoon, BH Park, J Shim, YO Han, BJ Hong, and SH Yun, "Numerical simulation of three-dimensional external gear pump using immersed solid method," Applied Thermal Engineering **118**, 539–550 (2017).

[17] C Kato, M Kaiho, and A Manabe, "An Overset Finite-Element Large-Eddy Simulation Method With Applications to Turbomachinery and Aeroacoustics," Journal of Applied Mechanics **70**, 32 (2003).

[18] CS Peskin, "Flow patterns around heart valves: A numerical method," Journal of Computational Physics **10**, 252–271 (1972).

[19] D Goldstein, R Handler, and L Sirovich, "Modeling a No-Slip Flow Boundary with an External Force Field," Journal of Computational Physics **105**, 354–366 (1993).

[20] G Iaccarino, G Kalitzin, and CJ Elkins, *Numerical and experimental investigation of the turbulent flow in a ribbed serpentine passage*, Tech. Rep. (Stanford, CA, 2003).

[21] G Iaccarino and R Verzicco, "Immersed boundary technique for turbulent flow simulations," Applied Mechanics Reviews **56**, 331 (2003).

[22] R Mittal and G Iaccarino, "Immersed Boundary Methods," Annual Review of Fluid Mechanics **37**, 239–261 (2005), arXiv:1007.1228 .

[23] CE Brennen, *Oxford Engineering Science Series*, Vol. 44 (1995) p. 304.

[24] JL Reboud, B Stutz, and O Coutier-Delgosha, "Two phase flow structure of cavitation: experiment and modeling of unsteady effects," 3rd International Symposium on Cavitation CAV1998 (1998).

[25] Ansys, "ANSYS FLUENT Theory Guide," (2017).

[26] D Wilcox, "Turbulence modeling for CFD," La Canada Flintridge, CA: D C W Industries (2006).

[27] A Prosperetti and G Tryggvason, *Computational methods for multiphase flow* (2009).

[28] M Holmgren, "X-Steam v2.6," .

[29] MG Mithun, P Koukouvinis, and M Gavaises, "Numerical simulation of cavitation and atomization using a fully compressible three-phase model," Physical Review Fluids **3**, 064304 (2018).

[30] MG Mithun, P Koukouvnis, IK Karathanassis, and M Gavaises, "Simulating the Effect of In-Nozzle Cavitation on Liquid Atomisation Using a Three-Phase Model," in *Proceedings of the 10th International Symposium on Cavitation (CAV2018)*, (ASME, New York, NY, 2018).

[31] A Roger Ull, "Study of mesh deformation features of an open source CFD package and application to a gear pump simulation," (2012).

[32] F Örley, V Pasquariello, S Hickel, and NA Adams, "Cut-element based immersed boundary method for moving geometries in compressible liquid flows with cavitation," Journal of Computational Physics **283**, 1–22 (2015).

[33] J Stryczek, P Antoniak, O Jakhno, D Kostyuk, A Kryuchkov, G Belov, and L Rodionov, "Visualisation research of the flow processes in the outlet chamberoutlet bridgeinlet chamber zone of the gear pumps," Archives of Civil and Mechanical Engineering **15**, 95–108 (2015).

[34] M Eaton, PS Keogh, and KA Edge, "The Modelling, Prediction, and Experimental Evaluation of Gear Pump Meshing Pressures with Particular Reference to Aero-Engine Fuel Pumps," Proceedings of the Institution of Mechanical Engineers, Part I: Journal of Systems and Control Engineering **220**, 365–379 (2006), arXiv:0803973233.

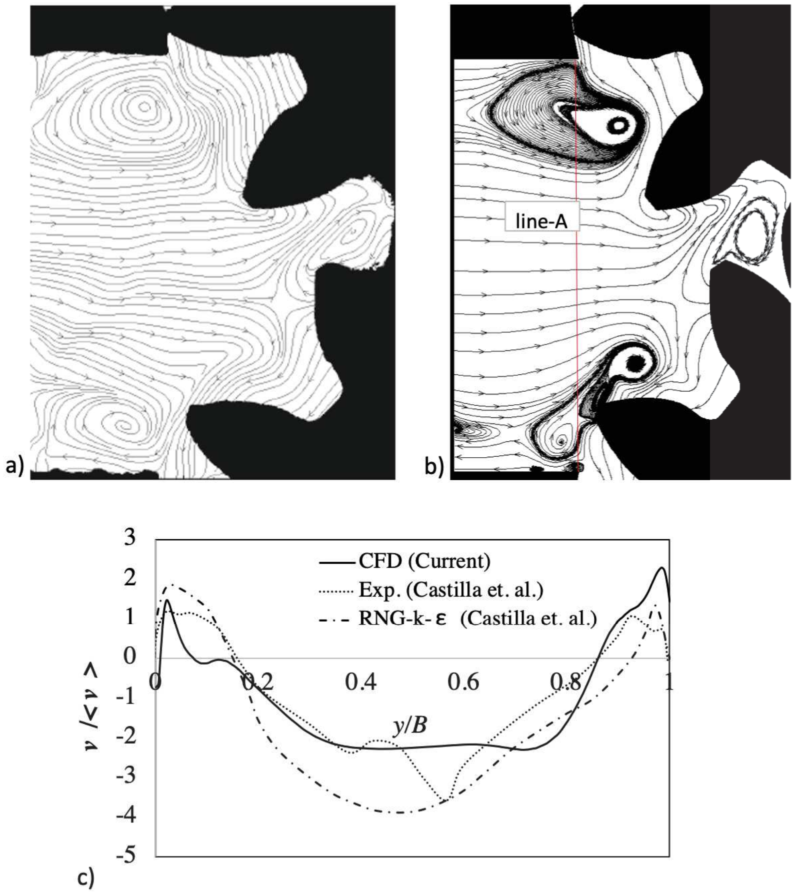

Figure 3: Comparison of the streamlines obtained by a) Castilla *et al.* [10] using TRPIV and b) the current numerical model using oil as working fluid, c) the velocity profile along line-A

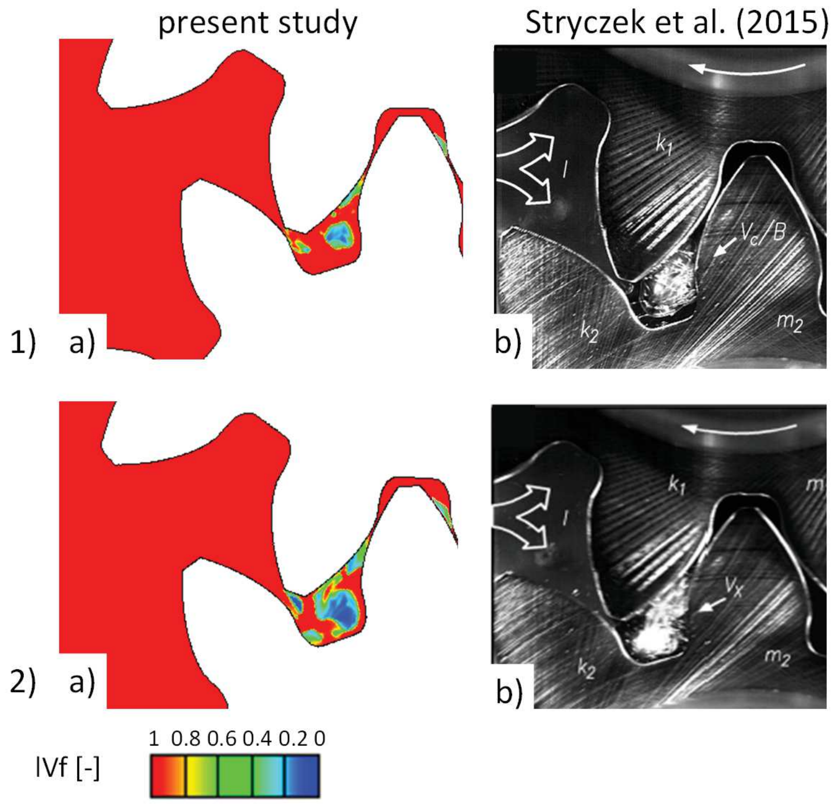

Figure 4: Comparison of the liquid volume fraction 1) at 500 RPM and 2) 1000 RPM; a) from the present simulation and b) from the experimental work of Stryczek *et al.* [33] to highlight cavitation occurring in the gap between gear teeth in the suction side. T_g is the time for one gearing period

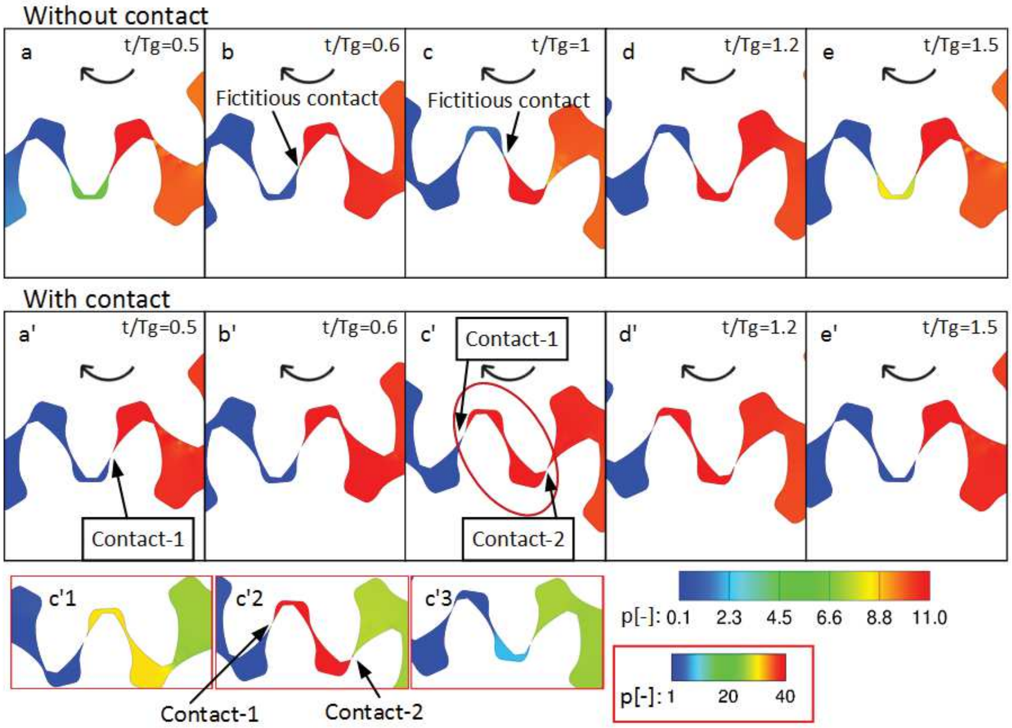

Figure 5: Comparison of non-dimensional absolute gauge pressure over a gearing period with (a-e) clearance between the gears and (a' - e') with contact between gears. The contours in the subset shows (c'1) the condition before the second contact, (c'2) pressure rise during two contacts in the isolated region and (c'3) the condition after the release of the first contact. Note that c' and c'2 corresponds to the same gear position. The time interval between the contour plots from a-e are not uniform; they are chosen to highlight specific events over a period

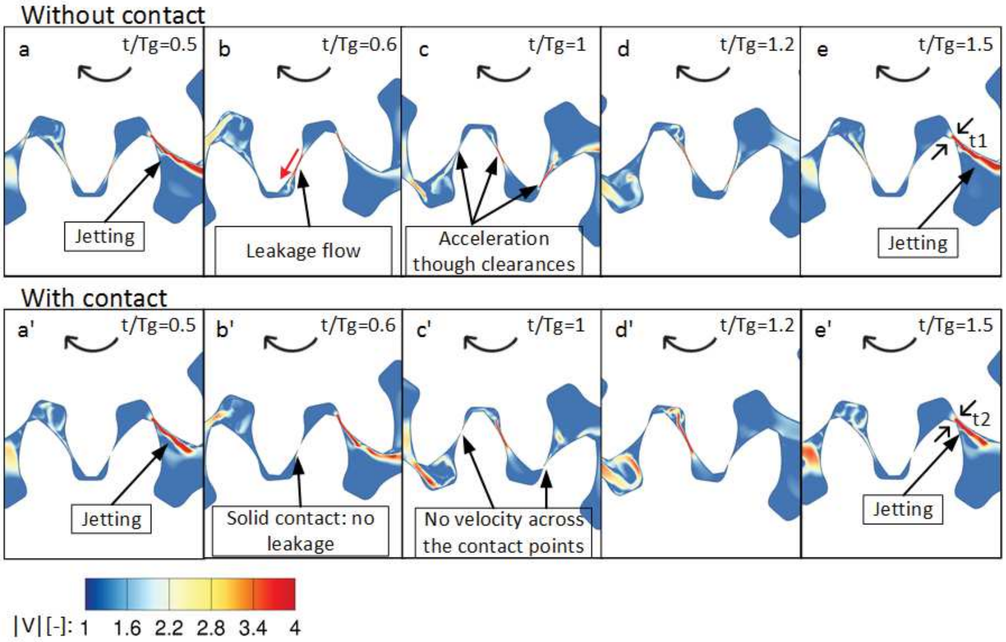

Figure 6: Comparison of non-dimensional velocity magnitude over a gearing period with (a-e) clearance between the gears and (a' - e') with contact between gears. The time interval between the contours from a-e are not uniform; they are chosen to highlight specific events over a period.

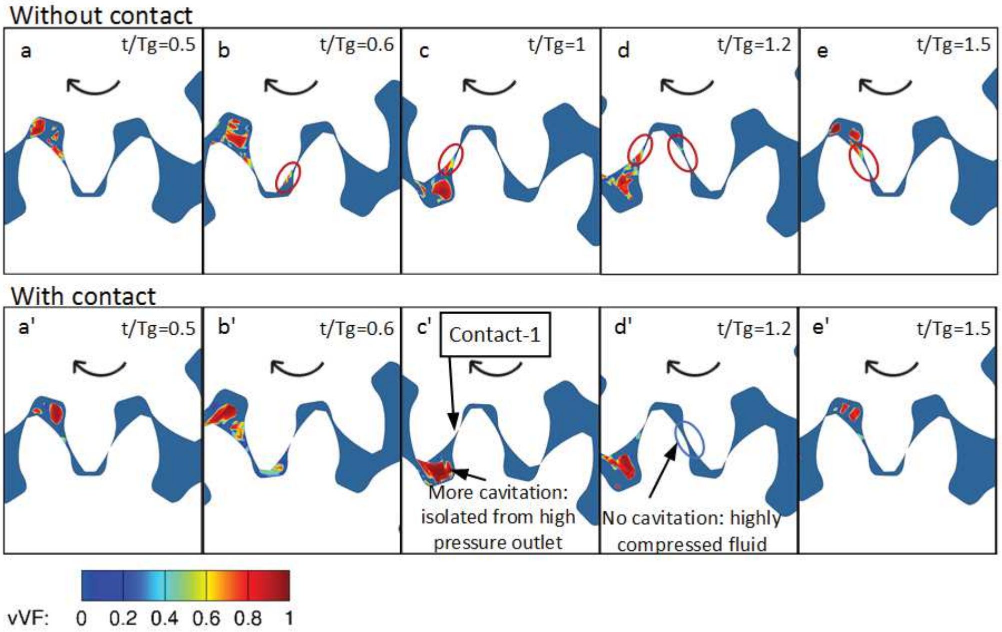

Figure 7: Comparison of vapour volume fraction over a gearing period with (a - e) clearance between the gears and (a' - e') with contact between gears. The time interval between the contours from a-e are not uniform; they are chosen to highlight specific events over a period

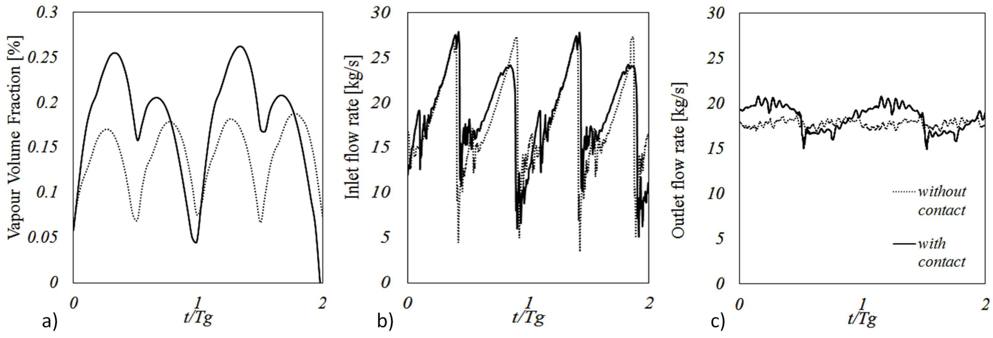

Figure 8: Comparison of a) area integral of vapour volume fraction normalised using the total flow area b) inlet flow rate and c) outlet flow rate over two gearing periods

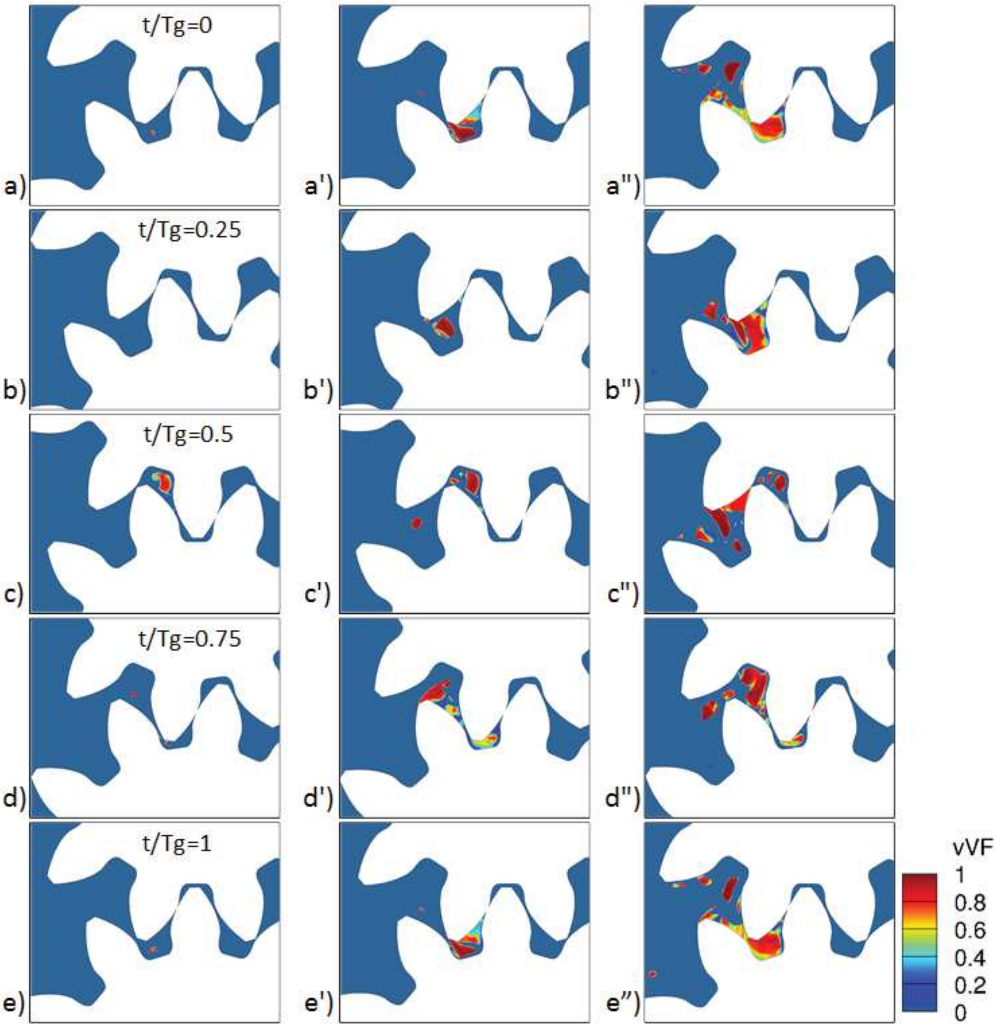

Figure 9: Comparison of cavitation formation at 500 RPM (a-e), 1000 RPM (a' - e') and 2000 RPM (a" - e") represented as contours of vapour volume fraction over one gearing period.

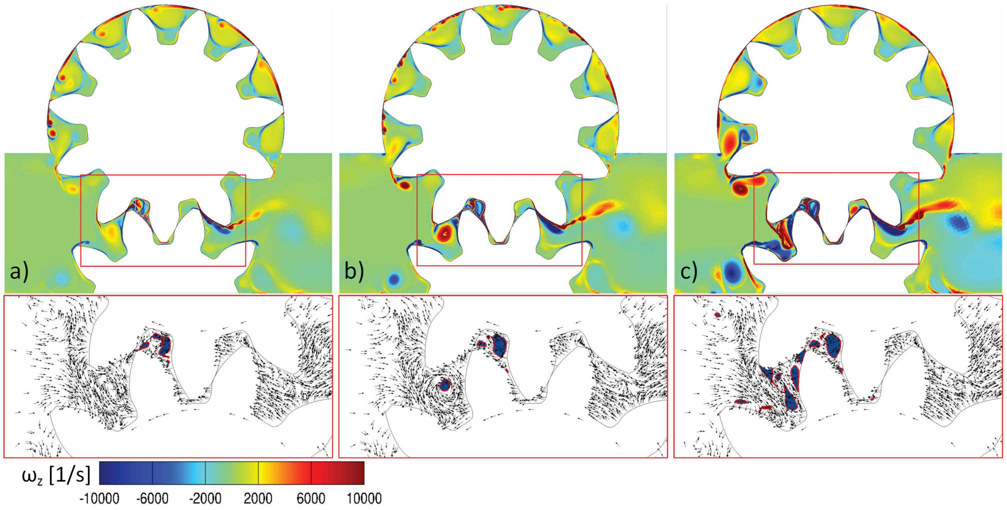

Figure 10: Contours of z-vorticity near the gearing zone and tip clearances at a) 500 RPM b) 1000 RPM and c) 2000 RPM. The normalised velocity vector along with 50% vapour volume fraction (blue) highlighting the two-dimensional vortex structures and locations of cavitation are given in the subset

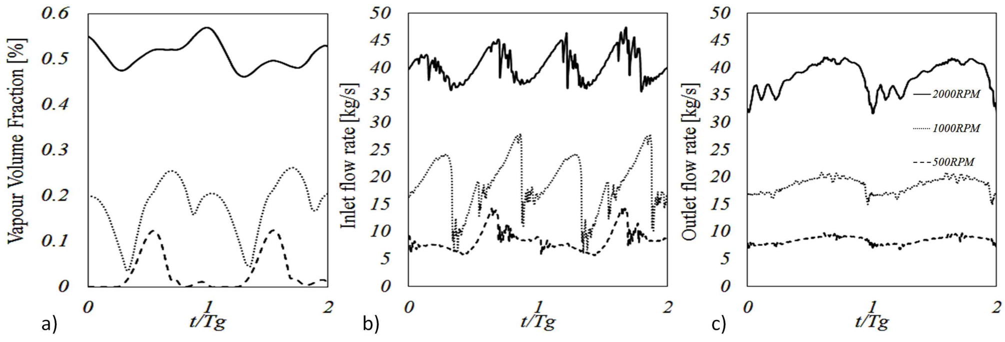

Figure 11: Comparison of a) area integral of vapour volume fraction normalized using the total flow area, b) inlet flow rate and c) outlet flow rate over two gearing periods at different gear RPM's

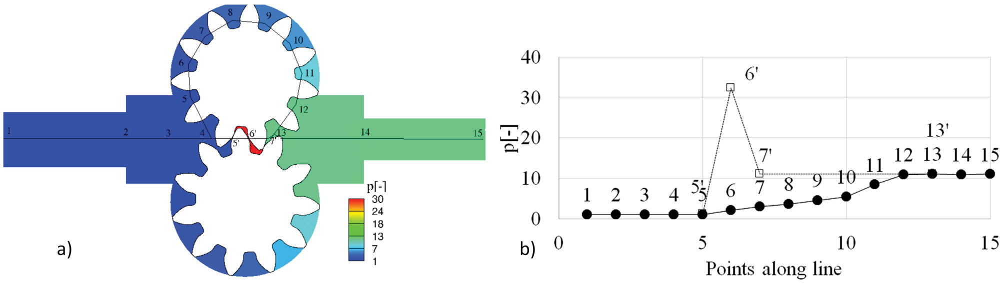

Figure 12: Representation of stairway pressure rise across inlet and outlet along the gear pockets at 500 RPM a) pressure contours with multiple locations along the line where the pressure is measured and b) the non-dimensional pressure at different points shown in (a)

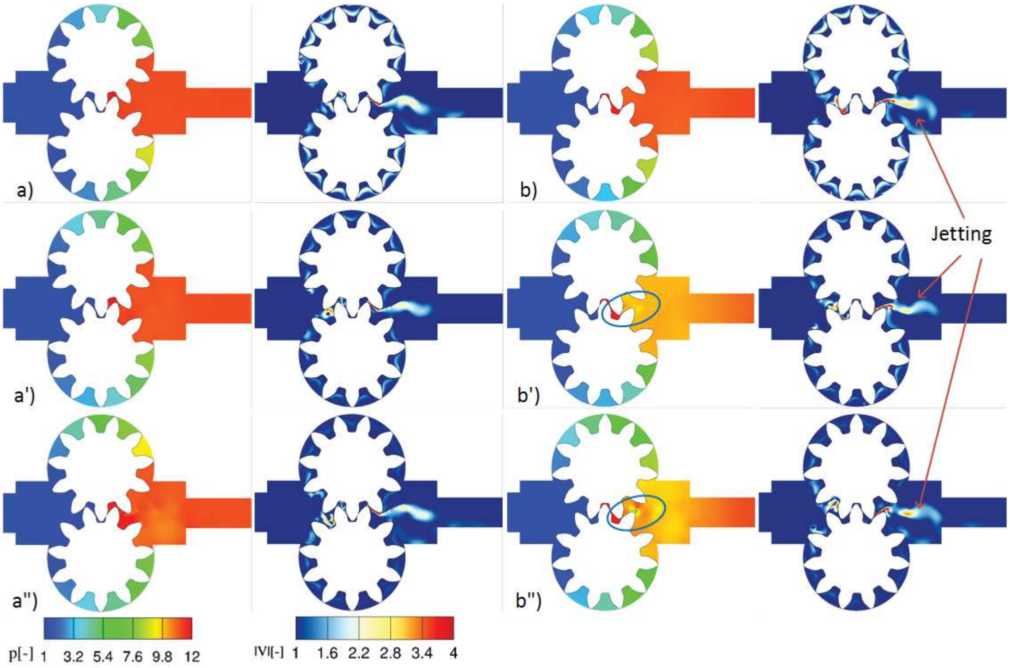

Figure 13: Contours of pressure and velocity magnitude 1) 500 RPM 2) 1000 RPM and 3) 2000 RPM and a)t/T_g=0 ie.(θ=0) and b) t/T_g=0.5 ie.(θ=0.5× $2\pi/11$)

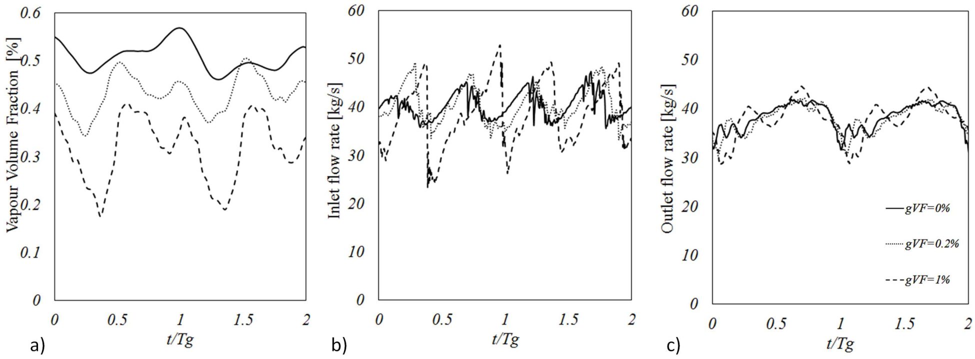

Figure 14: Comparison of the area integral of vapour volume fraction normalized using the total flow area over two gearing periods with different percentage of gas volume fraction at 2000 RPM.

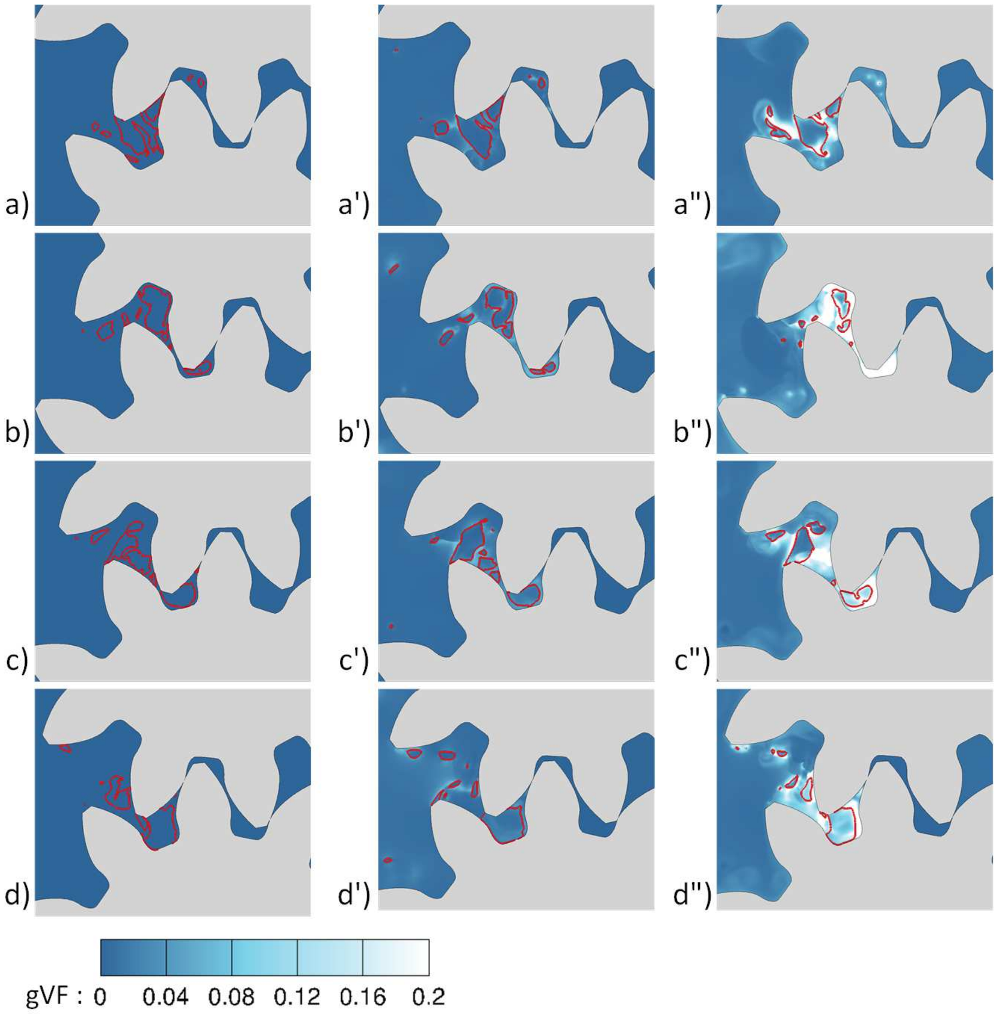

Figure 15: Evolution of NCG and cavitation; (a-d) for 0% NCG, (a'-d') for 0.2% and (a"-d") for 1% NCG content. The iso-lines of 50% vapour volume fraction shown in red lines. The instances are chosen randomly to highlight main features over a gearing period